Project Number: ERT _ MQP _ 12Q2

ANALYSIS OF ACTIN FILAMENT BENDING IN GLIDING ASSAYS

Major Qualifying Project Report completed in partial fulfillment
of the Bachelor of Science degree at
Worcester Polytechnic Institute

Pattipong Wisanpitayakorn

April 25, 2013

Professor Erkan Tüzel, Advisor
Department of Physics

Abstract

Gliding assays have been the standard tools of the past two decades to analyze the properties of molecular motors. Recently, we have shown that they can be used as model systems to study bending of bio-filaments. There are several approaches in the literature to measure filament deformations. One of the most commonly used approaches is Fourier analysis. In this project, we investigate this technique in great detail using computer simulations, and compare it with another novel technique, namely curvature distributions. We also compare our theoretical predictions and simulation results with experimental measurements of filament bending from actin gliding assays.

Contents

List of Figures

Acknowledgements

I would like to acknowledge Professor Erkan Tüzel and Professor Luis Vidali, as well as members of the Tüzel group James Kingsley and Göker Arpağ.

Chapter 1

Introduction

Microtubules and actin filaments are rigid tubular structures in cells that act like molecular highways to transport cellular signals and cargo. They also play an important role in cell division. Figure 1.1 shows a cartoon of an animal cell that contains microtubules and actin filaments. While microtubules are hair-like in terms of their aspect ratio, they have large resistance to bending, same as Plexiglass [1]. Actin filaments on the other hand are a lot softer, and they are responsible for the crawling motion of cells, and are also the fibers that contract in muscles [2]. During cell division, these bio-filaments inside the cell will change their form and shape. For example, in animal cells, microtubules bend and align to form the mitotic spindle, which brings chromosomes together during cell division [2]. Thus, it is important to study the mechanical behavior these filaments in order to understand their function as dynamic mechanical components in living cells. Current advancements in imaging techniques allow researchers to visualize these filaments, however, it is still difficult to experimentally identify the variety of molecular motors that exert forces on these filaments. Our long-term goal is to use the filament data obtained from fluorescence imaging to learn more about the forces acting at the molecular level and help identify the motors that exert forces.

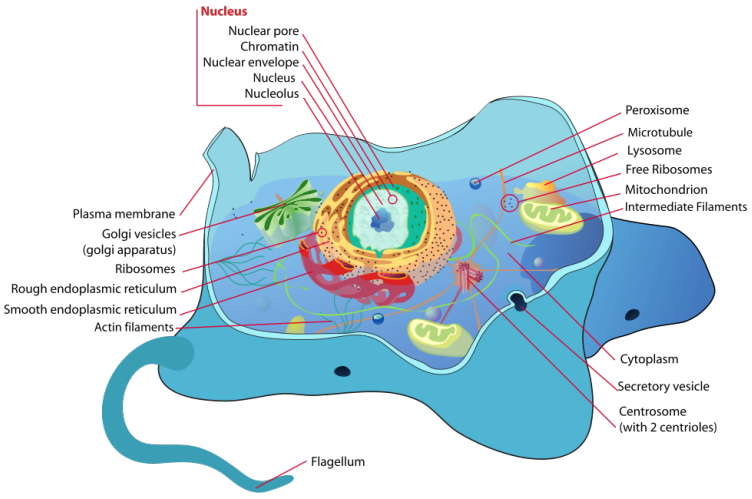

Figure 1.1: A cartoon showing microtubule and actin filaments found inside a eukaryotic animal cell. Image by Ruiz [3].

1.1 Cytoskeletal filaments

Cytoskeletal filaments can be grouped into three major types: microtubules, actin filaments and intermediate filaments. Since these filaments were discovered, the constituent proteins of those filaments have been chemically purified, and the proteins have been polymerized in the test tube to give filaments that are identical to those *in vivo* [2]. The atomic structures of these filaments have also been studied and used to build molecular models of the entire filaments [4]. The mechanical properties and organization of these filaments have a considerable effect on the mechanical properties of cells. This is especially true for animal cells, which have no cell walls and the mechanical rigidity of the cell is reinforced by the microtubule cytoskeleton [5]. Moreover, cytoskeletal filaments are also crucial for the internal organization of cells. For example, actin filaments and microtubules are used as tracks for the molecular motor proteins to move vesicles and organelles in the cells with high efficiency [2].

1.1.1 Microtubules

Microtubules have a crucial organizational role in all eukaryotic cells. They are long and stiff hollow tubes. They can rapidly disassemble and reassemble, a process called dynamic instability [6]. They are composed of many tubulin subunits with a characteristic scale length of 8 nm. Purified tubulin subunits in a test tube will spontaneously assemble to form microtubules under appropriate conditions [6]. Microtubules are hollow cylindrical structures with the inner diameter of about 18 nm and the outer diameter of about 25 nm [2]. The cross sections of microtubules are one layer ring composed of 13 tubulin subunits. The dimers self-assemble longitudinally along the length of the microtubules to form a protofilament. Each protofilament has a structural polarity, with α-tubulin exposed at one end and β-tubulin exposed at the other. In Figure 1.2, the protofilaments connect laterally to each other to form a sheet that closes to form the cylindrical tube, microtubule. Most cellular microtubules have 13 protofilaments with 3 starts, meaning that it can be thought of as helices with 3 strings of monomers connected to each other. Since the polarity is the same for all protofilaments, the microtubule as a whole also has polarity [2].

Microtubules are key in many cellular processes. They serve as a conduit for the motion of molecular motors such as kinesin and dynein for directed intracellular movements. Once these molecular motors bind to a microtubule, they use the energy obtained from repeated cycles of ATP hydrolysis to move along the microtubules in one direction. At the same time, these motor proteins also attach to the other cellular components in order to transport these cargos along the filaments. Microtubules also control the organization of cell division. During mitosis, the microtubules inside the cell cytoplasm disassemble and then reassemble into a structure called the mitotic spindle, which segregates chromosomes equally into the two daughter cells just before a cell divides [2]. Microtubules can also form permanent structures, such as the core of the hair-like structures called cilia and flagella [6]. These extend from the surface of several eukaryotic cells, which is used either for propulsion or to sweep fluid over the cell surface. In a cell, microtubules are sometimes found in bundles. For example, in the mitotic spindle, each chromosome is attached to a bundle of approximately 30 microtubules that are all oriented in the same direction and cross-linked together in order

to separate and duplicate chromosome during cell division [7].

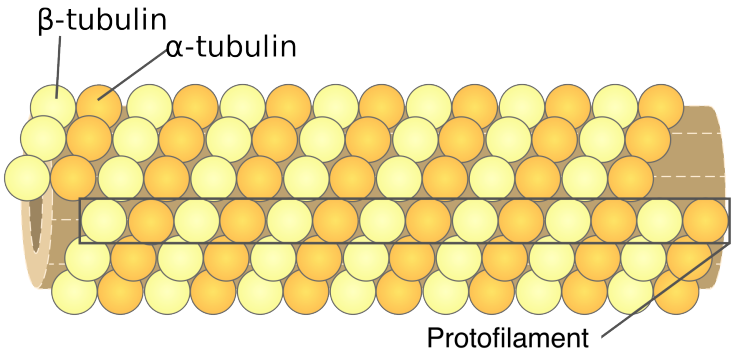

Figure 1.2: The hollow tube-like structure of a microtubule. Rectangular box shows a protofilament, self-assembled by repeated tubulin dimers. Image by Zlira [8].

1.1.2 Actin Filaments

Actin Filaments are found in all eukaryotic cells and are essential for many of their movements. Like microtubules, actin filaments are helical assemblies of globular subunits, actin monomers. The actin monomers form a one-start, left-handed helix to create the filament structure. Even though the full period of the actin filaments is 72 nm, the repeats can be seen as 36 nm under the electron microscope, because the image of the filament is projected onto the plane. One full period has 26 subunits, which makes 13 complete turns. Therefore, the diameter of each subunit is 2.77 nm [9]. Since the monomers assemble into the helix form, the length between the longitudinal adjacent subunits is 5.54 nm, or twice the size of the subunit. Even though an actin monomer has nearly the same size as a tubulin subunit, the actin filaments are a lot softer than a microtubule, since each of them consists of only 2 protofilaments stranding with each other rather than 13 as shown in Figure 1.3. Actin filaments appear in electron micrographs as threads about 6 nm in diameter [4]. Because the actin monomers are asymmetrical, the actin filaments have a distinct polarity and their ends are structurally different. This polarity leads to faster polymerization at one end than the other. The fast-growing end is called the plus end, whereas the slow-growing end is called the minus end [2].

Inside cells, actin filaments are often found in bundles. They serve a variety of roles in cells, with some of its most familiar activities related to motility. Without actin filaments, an animal cell could not crawl along a surface, or divide in two [6]. Even though many actin filaments are unstable, they can form stable structures in cells, such as the contractile apparatus of muscle [10]. Actin filaments are associated with a large number of actin-binding proteins, the myosin family [2]. Depending on their association with different proteins, actin filaments can also form stiff and quite permanent structures, such as the microvilli on the brush-border cells lining the intestine or small contractile bundles in the cytoplasm. These microvilli contract and act like the "muscles" of a cell. Actin filaments can also form temporary structures, such as the protrusions formed at the leading edge of a crawling fibroblast or the contractile ring that pinches the mother cell into two daughter cells during animal cell division [6].

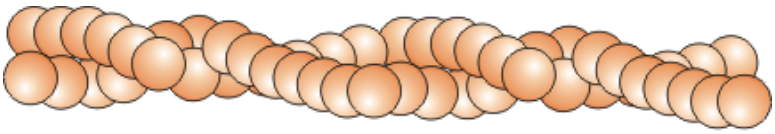

Figure 1.3: Two protofilaments form a strand of actin filament. These protofilaments are made of many actin monomers bind to each other forming a string like structure. Image by Boumphreyfr [11].

1.1.3 Intermediate Filaments

Intermediate filaments are found in the cytoplasm of most animal cells. They normally form a network inside the cytoplasm, surrounding the nucleus and extending out to the cell periphery. The structures of intermediate filaments are very different from those of microtubules and actin filaments. The subunits of the intermediate filaments are elongated proteins rather than globular. Those proteins assemble into intermediate filaments based on lateral bundling and twisting into coiled-coil structures [2]. Figure 1.4 shows the assembly of elongated proteins forming a dimer and tetramer. One role of the intermediate filaments in the cells is to provide mechanical resistance to stretching of the cells in tissues. These coiled-coil dimers join to form antiparallel tetramers that are wound together in a rope-like structure that lends them their mechanical strength [7].

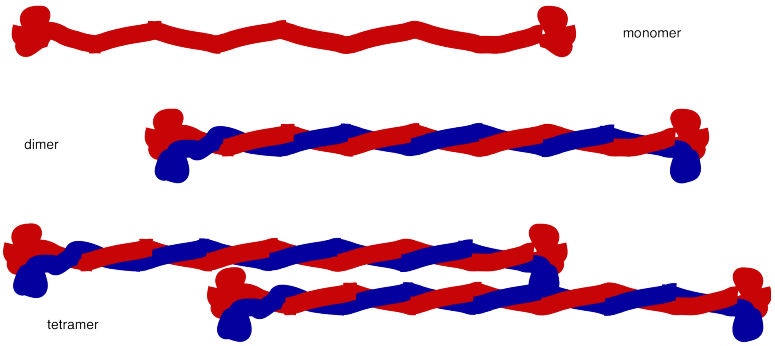

Figure 1.4: A sketch showing protein subunits assembling into intermediate filaments. Image by Haggstrom [12].

1.2 Quantifying Deformations of Bio-filaments

Microtubules and actin filaments resist various forces to maintain cell shape and help motor proteins generate force for cell movements and changes in cell shape. While doing so, these filaments continuously bend and buckle, and therefore a filament's resistance to bending is an important quantity to measure. One way to characterize the bending deformations of these filaments is to measure the *persistence length*, the length scale over which thermal

fluctuations can cause the filaments to spontaneously bend [13]. While there have been many measurements of the persistence length of these bio-filaments *in vitro* [14], to the best of our knowledge, such measurements have not yet been conducted successfully *in vivo*. In addition, in living cells, these filaments can potentially have defects and associated proteins that can bind and change local resistance to bending, making the determination of persistence length more difficult [7]. It is therefore very important to develop new techniques to measure the persistence length of such filaments, particularly *in vivo*.

As we will discuss in great detail in Chapter 2, the persistence length of a filament is also related to its flexural rigidity. One of the first estimation of microtubule flexural rigidity *in vitro* made use of statistical measurement of microtubule curvature in electron microscopic images [15]. Since then, microtubule flexural rigidity has been further estimated from dynamic video images using various techniques. Although these methods are based on the same mechanical principle, they are different depending on the following: whether the analysis involves classical mechanics, statistical mechanics or hydrodynamics; the type of working force on the microtubule; the balance and direction of working forces and the microtubule internal stiffness; and the number of force fulcrums [16]. A brief description of different approaches, along with their strengths and weaknesses will be discussed in the following.

1.2.1 Spectral Analysis Approach

The strategy for measuring the flexural rigidity of bio-filaments with this technique is to resolve the thermal bending of a single filament. The shape of the filament is characterized as a sum of cosine waves of increasing frequency [1] (see Figure 1.5). This technique is called Fourier decomposition. Here, the amplitude of each Fourier mode depends on the filament's shape. As the filament changes shape over time due to thermal fluctuations, the amplitude of each mode fluctuates as well. The variance of the amplitude of the modes can then be used to estimate the flexural rigidity of the filament. The details of this approach will be discussed later in Section 2.2. Fourier analysis can provide an accurate estimation for both stiff filaments such as microtubules, and softer filaments, *i.e.* actin. Nevertheless, this technique requires fluctuating microtubules to have similar lengths with both ends free to wiggle.

1.2.2 Buckling Force Measurements Using Optical Traps

This method is based on the classical mechanics problem of buckling of beams under an external force. A filament is balanced at force fulcrums using an optical trap, and the minimum force required for a filament to buckle is measured. In this technique, each end of the filament is bound to an anti-tubulin-coated bead (in the case of a microtubule) to improve specific and stable immobilization between the beads and the microtubule. Then, both of the beads are trapped in a focused laser beam and are moved closer to each other by applying adjustable identical forces as shown in Figure 1.6. The applied forces and the bending angle along the filament can be used to obtain the flexural rigidity of the filament [16]. This method involves relatively simple mechanical analysis since there are only two working forces that do not change over time. This buckling force measurement may be considered to be the

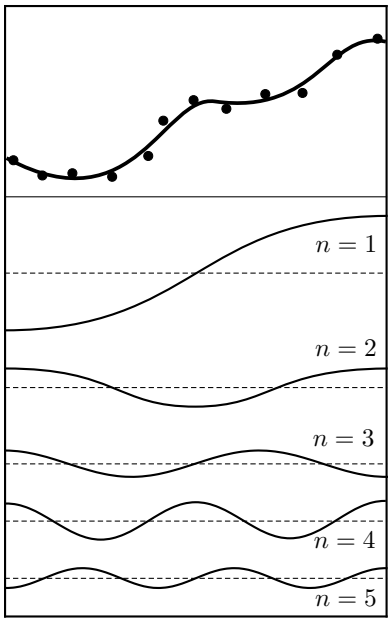

Figure 1.5: An illustration of Fourier decomposition. With no boundary conditions imposed on the filament, the shape of filament can be represented by a sum of cosine modes with different amplitudes.

most direct technique to measure filament rigidity because it employs the fewest number of assumed parameters. However, it is difficult to control the boundary conditions of the measurement. The fluctuation in the trapping force and thermal fluctuations can also cause a significant error.

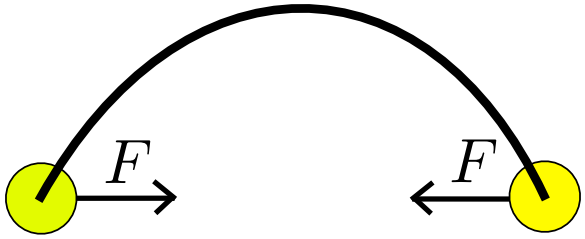

Figure 1.6: A sketch of the optical trap setup. Both ends of a bio-filament are trapped using laser beams. The beams are then brought closer together to generate the force that makes them buckle.

1.2.3 Calibrated Hydrodynamic Flow

In this technique, filaments are nucleated while anchored to a glass coverslip on one end. A constant flow of buffer is then imposed on the filament to observe its resistance to bending. The flexural rigidity of the filament can then be calculated using the amount of deflection of the filament [17]. Again, this technique can be performed only *in vitro*, since it requires

very specific circumstances, such as the filaments being under some constant flow of fluid with a known flow rate, which is very difficult to obtain within the complex and crowded environment of the cell.

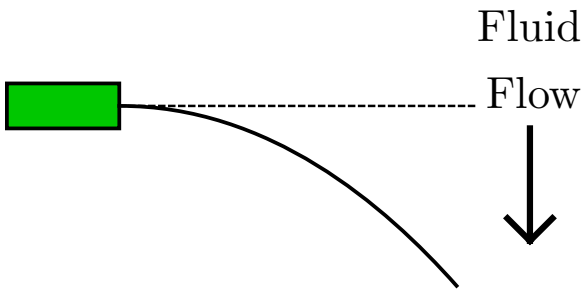

Figure 1.7: A sketch of the calibrated flow technique. A constant flow of fluid is imposed on a filament with one end bound to an immobile object.

1.2.4 Curvature Distributions

While there are a good number of techniques to measure the flexural rigidity of microtubules and actin filaments *in vitro* [14], some of which we have briefly reviewed here, existing approaches are not readily applicable *in vivo* due to the complexity of forces and the boundary conditions involved, and the crowded environment in a cell. Therefore, there is need for a new technique that can break through those limitations in order open the possibility of measuring the bending properties of the bio-filaments in a living cell. A promising approach that has been useful in a number of studies to quantify the bending of bio-filaments *in vivo* is the use of curvature distributions [18, 19, 20]. However, this approach needs to be investigated further in order to determine its range of applicability as a viable tool to measure bending in living.

1.3 Summary

Cytoskeleton is the cellular skeleton within a cell. It plays numerous important roles in cells and determines the mechanical properties of cells. Cytoskeletal filaments, such as microtubules or actin filaments take part in a variety of cellular processes ranging from cellular division to motility. Since these filaments deform continuously in a living cell, it is important to understand how they bend as a result of the forces they are subject to. In the literature, there are a number of techniques available to measure the flexural rigidity of bio-filaments, spectral analysis, optical traps to name a few. However, these techniques are difficult to use in living cells. There is a need, therefore, for better and more accurate approaches for *in vivo* characterization of bending. In Chapter 2, starting with the formal definitions of bending energy, we will discuss in detail two of these approaches, namely spectral analysis and curvature distributions. In Chapter 3, we will present our results from Monte Carlo simulations and analysis of the experimental data for both the Fourier

and curvature analysis. We will end this report with conclusions and future directions in Chapter 4.

Chapter 2

Quantification of Bio-filament Bending

In this chapter, we will introduce the theory necessary to characterize bending deformations. We will define concepts like persistence length to flexural rigidity mathematically, and introduce two techniques used for measuring persistence lengths, namely Fourier analysis and curvature distribution.

2.1 Mechanics of Bending

2.1.1 Bending Energy

Since bio-filaments are long repeating monomers, whether they are made up of actin subunits or tubulin, they can be modeled as a continuous string with resistance to bending (see Figure 2.1). In our model, we will assume that the filament is inextensible, hence explicit stretching energy. Figure 2.1 shows a thin semi-flexible rod of fixed length L on a plane and its shape can completely be represented by the tangent angle $\theta(s)$ at every point s along the rod of length $L(0 < s \leq L)$. The curvature at each point along the rod is given by $d\theta/ds$. If the radius of curvature is much greater than the filament diameter, we can write

$$\frac{dU}{ds} = \frac{1}{2} EI \left(\frac{d\theta}{ds} - \frac{d\theta^0}{ds} \right)^2 \tag{2.1}$$

where dU/ds is the bending energy per unit length and $\theta^0(s)$ is the shape of the relaxed rod due to intrinsic bending in the absence of applied or thermal forces [2]. Here the product EI is called the flexural rigidity, composed of the Young's modulus (E) and the second moment of cross-sectional area (I). Note that here we assume the rod is made of an isotropic elastic substance. The second moment of cross-sectional area is given by

$$I = \int_A y^2 dA \ . \tag{2.2}$$

Integrating over Eq. (2.1), one can get the total energy of bending for an infinitely thin rod in the plane, *i.e.*

$$U = \frac{1}{2} EI \int_0^L ds \left(\frac{d\theta}{ds} - \frac{d\theta^0}{ds} \right)^2 \quad . \tag{2.3}$$

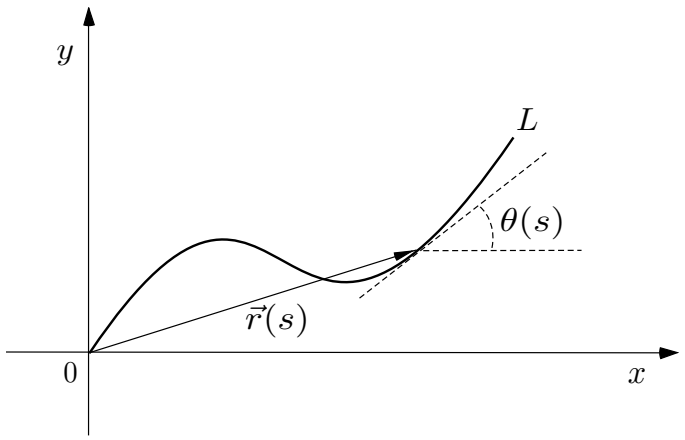

Figure 2.1: A filament can be modeled as a continuous string with resistance to bending.

2.1.2 Persistence Length

To find the relationship between the persistence length (L_p) and the flexural rigidity (EI) of an elastic beam, we take a short beam of length $s \ll L_p$ and compute $g(s)$, the tangent-tangent correlation function. For such a beam of arc length of s (as shown in Figure 2.2), the bending energy in Eq. (2.3) can be written as

$$U_{bend} = \frac{EI}{2s} \theta^2 \tag{2.4}$$

with $\theta = s/R$. To compute the persistence length, we start from the tangent-tangent correlation function along a filament given by

$$g(s) = \langle t(s) \cdot t(0) \rangle \tag{2.5}$$

where $t(s) = \partial \vec{r}(s)/\partial(s)$. Taking the tangent of one end of the beam to point along the $\hat{z}$-direction, the tangent-tangent correlation function becomes

$$g(s) = \langle \cos \theta(s) \rangle \quad . \tag{2.6}$$

If we assume that the deflection angles are very small, *i.e.* $\theta \ll 1$, the cosine function can be expanded into Taylor series. Ignoring higher order terms, one arrives at the following simplified expression

$$g(s) = \langle 1 - \frac{\theta^2(s)}{2} \rangle \quad . \tag{2.7}$$

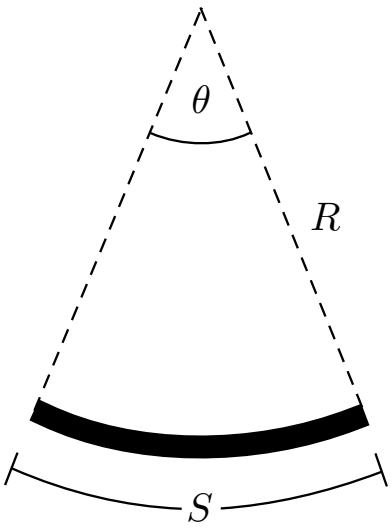

Figure 2.2: A short beam of arc length s.

The ensemble average in Eq. (2.7) is computed by summing over all possible orientations of the tangent vector at s, which in three dimensions traces out the surface unit sphere. Therefore, using Eq. (2.4) one can write

$$\langle \theta^2(s) \rangle = \frac{1}{\mathcal{Z}} \int_0^{2\pi} d\phi \int_0^{\pi} d\theta \sin\theta \;\; \theta^2 e^{-\frac{EI}{2k_B T s}\theta^2} \quad . \tag{2.8}$$

where

$$\mathcal{Z} = \int_0^{2\pi} d\phi \int_0^{\pi} d\theta \;\; \sin\theta \; e^{-\frac{EI}{2k_B T s}\theta^2} \tag{2.9}$$

is the normalization factor (partition function). Notice that the integrand in Eq. (2.8) differs from the partition function by the factor of θ^2 which can be pulled down from the expression in Eq. (2.9) by differentiating it with respect to E. Thus, we can write

$$\langle \theta^2(s) \rangle = \frac{1}{\mathcal{Z}} \left(-\frac{2\pi k_B T s}{I} \;\; \frac{\partial \mathcal{Z}}{\partial E} \right) = -\frac{2\pi k_B T s}{I} \;\; \frac{\partial \ln \mathcal{Z}}{\partial E} \quad . \tag{2.10}$$

For small angles, we can assume that $\sin\theta \approx \theta$ and do the integration in Eq. (2.9) by making a change of to variable $u = (EI/2k_BTs)\theta^2$, obtaining

$$\mathcal{Z} = \frac{2\pi k_B T s}{EI} \int_0^{\infty} du \; e^{-u} = \frac{2\pi k_B T s}{EI} \quad . \tag{2.11}$$

Equation (2.10) can be used to obtain an expression for the mean-squared average of the angle $\theta(s)$, *i.e.*

$$\langle \theta^2(s) \rangle = \frac{2k_B T s}{EI} \quad . \tag{2.12}$$

After substituting this result into the simplified Taylor expansion of the tangent-tangent correlation function, we arrive at the result

$$g(s) = 1 - \frac{k_B T}{EI} s \quad . \tag{2.13}$$

The tangent-correlation function in Eq. (2.13) looks similar to the Taylor expansion for an exponential function. Also, our tangent vector is of unit length, $g(0) = 1$. On the other hand, we expect that the two tangent vectors will be independent for s much larger than the persistence length and $g(s) \to 0$. Therefore, one can arrive at the conclusion that the tangent-tangent correlation function is an exponential function of the form

$$g(s) = e^{-\frac{k_B T}{EI} s} \quad . \tag{2.14}$$

Since the factor in front of s in the exponential form characterizes how quickly the shape changes along the filament, this factor is taken as the definition for the persistence length. Equation (2.14) can now be rewritten as

$$g(s) = e^{-s/Lp} \quad , \tag{2.15}$$

where

$$L_p = \frac{EI}{k_B T} \quad , \tag{2.16}$$

is the persistence length [7].

2.2 Fourier Analysis Technique

2.2.1 Decomposition of Filament Shape into Cosine Modes

Using Fourier analysis, we can express the filament shape, characterized by $\theta(s)$, as a superposition of Fourier modes, *i.e.*,

$$\theta(s) = \sum_{n=0}^{\infty} \theta_n(s) = \sqrt{\frac{2}{L}} \sum_{n=0}^{\infty} a_n \cos(\frac{n\pi s}{L}) \quad . \tag{2.17}$$

Since there are no boundary conditions imposed on $\theta(s)$, we can use a cosine only expansion for computational convenience. A sine or mixed sine and cosine expansion would fit this task perfectly as well. Equation 2.17 is then differentiated and plugged into Eq. (2.3). As a result, the zero-mode magnitude will vanish, so that we can start summing from the first mode to infinity. This yields

$$U = \frac{1}{2} EI \sum_{n=1}^{\infty} \frac{2}{L} \left(\frac{n\pi}{L}\right)^2 (a_n - a_n^0)^2 \int_0^L ds \sin^2(\frac{n\pi s}{L}) \quad . \tag{2.18}$$

After evaluating the integrant, the energy of bending in Eq. (2.3) can now be written as a quadratic summation of these coefficients

$$U = \frac{1}{2} EI \sum_{n=1}^{\infty} \left(\frac{n\pi}{L}\right)^2 \left(a_n - a_n^0\right)^2 \quad . \tag{2.19}$$

Note that the zero-order mode (a_0) corresponds to the average orientation of the filaments and does not contribute to the bending energy. In equilibrium, the equipartition theorem [21] states that each quadratic term in Eq. (2.19) contributes an average $k_B T/2$. This implies that

$$var(a_n) = \langle (a_n - a_n^0)^2 \rangle = \frac{kT}{EI} \left(\frac{L}{n\pi}\right)^2 \quad . \tag{2.20}$$

The angle brackets denote an average over many configurations. The lack of cross-terms in the expression for energy implies that the quantities $(a_n - a_n^0)$ are uncorrelated for different values of n. Thus, the variation, or fluctuation, in amplitude of each mode ($n \geq 1$) provides an independent estimated of the flexural rigidity.

The thermal bending of flexible polymers is commonly discussed in terms of the persistence length $L_p = EI/k_B T$, which is the arc length above which the angle $\theta(s)$ becomes uncorrelated in three-dimensional motion. Using Eq. (2.20), once can relate the persistence length to the variance as

$$L_p = \frac{L^2}{n^2 \pi^2 var(a_n)} \quad . \tag{2.21}$$

2.2.2 Numerical Estimation of Filament Shape

To estimate the persistence length, L_p, using Eq. (2.21), we wrote an algorithm that performs Fourier analysis on a given set of filament contours—either experimentally or computationally generated. Consider a filament consisting of $N + 1$ points in two dimensions. From the set of N segments that connect these points, we can calculate the spacing between the bonds using

$$\Delta s_i = \left[(x_{i+1} - x_i)^2 + (y_{i+1} - y_i)^2\right]^{\frac{1}{2}} \tag{2.22}$$

and the tangent angles

$$\theta_i = \tan^{-1}\left(\frac{y_{i+1} - y_i}{x_{i+1} - x_i}\right) \quad . \tag{2.23}$$

However, using the *arctangent* function of Matlab alone would give us discontinuities in the angles for the filaments with small persistence length, which led to errors in our Fourier analysis. This is because the range of the arctangent function is in the interval $[-\pi/2, \pi/2]$. Thus, if the actual angle is in the 1^{st} quadrant, then it is equal to θ_i. If the angle is the 2^{nd} or 3^{rd} quadrants, then we add π to θ_i. Finally, for the 4^{th} quadrant, the angle is $2\pi + \theta_i$. In addition to these modifications, there might be cases in which one bond angle falls into the 1^{st} quadrant and the following bond angle falls into the 4^{th} quadrant. The reverse of this situation can also happen, in which we go from 4^{th} to the 1^{st} quadrant. To make sure this does not cause additional discontinuities in the angle θ_i, we keep a counter of such events,

and every time there is a jump from quadrant 4 to 1, we increment this counter by 2π. For the opposite case, we subtract 2π from this counter. The resulting value of the counter is then added to every angle θ in the next steps. The constructed vector of angles are then used in the Fourier analysis. The coefficients a_n can be calculated using

$$a_n = \sqrt{\frac{2}{L}} \int_{s=0}^{L} ds\ \theta(s)\ \cos\left(\frac{n\pi s}{L}\right) \quad , \tag{2.24}$$

which is obtained by taking an integral over Eq. (2.17) and using orthogonality relations for cosines and sines. In discrete form, Eq. (2.24) can be written as

$$a_n \ \cong\ \sqrt{\frac{2}{L}} \sum_{i=1}^{N} \Delta s_i\ \theta_i\ \cos\left(\frac{n\pi}{L} s_i^{mid}\right) \quad , n = 1, ..., N-1 \tag{2.25}$$

where

$$L = \sum_{i=1}^{N} \Delta s_i \tag{2.26}$$

and

$$s_i^{mid} \ =\ \Delta s_1 + \Delta s_2 + \ldots + \Delta s_{k-1} + \frac{1}{2}\Delta s_k \ . \tag{2.27}$$

In principle, the variance of each of these an values can be used to obtain an independent estimate of flexural rigidity, EI, via Eq. (2.21). Nevertheless, in experiments, measurement noise prevents accurate resolution of the higher order modes. In the next section, we will discuss how noise and pixelation errors can affect the accuracy of this approach, and how to remedy that.

2.2.3 Role of Pixelation

In experiments, data would suffer from the pixelation errors due to the limited resolution of the microscope: each measured point along the filament would deviate from the actual position on the filament by a random distance ϵ_k, as illustrated in Figure 2.3. This experimental error adds directly to the true variance of the amplitude of each mode, causing errors in the persistence length estimation. Therefore, the effect of this error needs to be taken into account in order to obtain an accurate persistence length from experimental data.

Since the curvature of the filament due to thermal fluctuation is considerably small, the pixelation error, ϵ_k, contribute to each a_n value. Let us assume that the measured coordinates of the filament line are straight and that the actual coordinates deviate from that line by ϵ_k, as shown in Figure 2.3. Assuming that all the bonds have equal length of Δs_0, when the ϵ_k are nonzero, the k^{th} bond has the length and angle

$$\Delta s_k \ =\ [\Delta s_0^2 + (\epsilon_{k+1} - \epsilon_k)^2]^{\frac{1}{2}} \ \cong\ \Delta s_0 \ , \tag{2.28}$$

$$\theta_k \ =\ \tan^{-1}\left(\frac{\epsilon_{k+1} - \epsilon_k}{\Delta s_0}\right) \ \cong\ \frac{\epsilon_{k+1} - \epsilon_k}{\Delta s_0} \ . \tag{2.29}$$

The assumption that all bonds are equal in length gives the midpoint of the k^th segment to be

$$s_k^{mid} \;=\; \frac{(k-\frac{1}{2})L}{N} \quad . \tag{2.30}$$

Thus, by plugging Eq. (2.28), (2.29) and (2.30) into Eq. (2.25), the error from deviation leads to the following modified amplitude for Fourier mode

$$a_n^{noise} \;=\; \sqrt{\frac{2}{L}} \sum_{k=1}^{N} (\epsilon_{k+1} - \epsilon_k) \; \cos\left[\frac{n\pi}{N}(k-\frac{1}{2})\right] \quad . \tag{2.31}$$

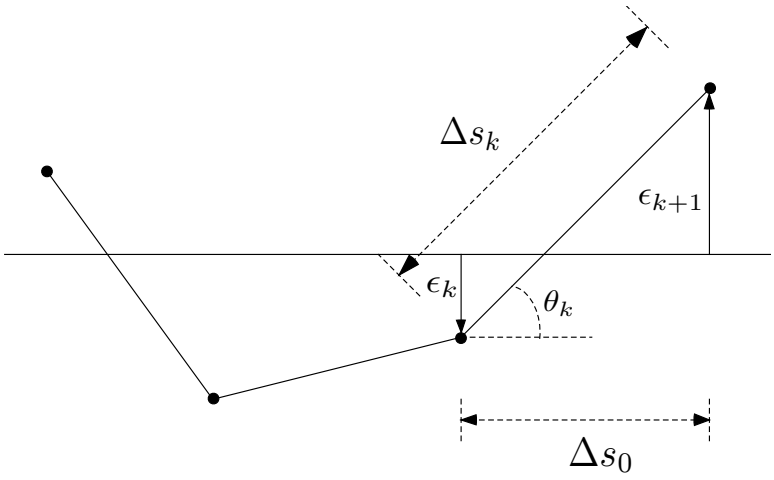

Figure 2.3: A sketch showing the definitions used to discuss pixelation errors.

We then rearrange the right hand side of Eq. (2.31) into terms of each distinct ϵ_k, using the fact that ϵ_k's are independent random variables. Also using the fact that

$$\sum_{k=1}^{N-1} \sin^2\left(\frac{n\pi k}{N}\right) \;=\; \frac{N}{2} \quad , \tag{2.32}$$

we obtain the expression for the noise variance for each mode amplitude to be

$$\langle a_n^2 \rangle^{noise} \;=\; \frac{4}{L}\langle \epsilon_k^2 \rangle \left[1 + (N-1) \; \sin^2\left(\frac{n\pi}{2N}\right)\right] \quad . \tag{2.33}$$

Therefore, we expect the measured $var(a_n)$ from the experimental data to be given by [1]

$$var(a_n)^{measured} \;=\; \left(\frac{L}{n\pi}\right)^2 \frac{1}{L_p} + \frac{4}{L}\langle \epsilon_k^2 \rangle \left[1 + (N-1) \; \sin^2\left(\frac{n\pi}{2N}\right)\right] \quad . \tag{2.34}$$

In a log-log plot of variance against mode number, the error term will contribute to the tail of the curve. We can then use this expression of $var(a_n)$, that includes noise and pixelation effects into account, to estimate the persistence length from experimental images. The experimentally measured variance can be fitted to Eq. (2.34) using the two parameters L_p and ϵ_k.

2.2.4 Algorithm for the Fourier Analysis Technique

The implementation of the Fourier analysis can be described briefly by the following pseudo algorithm.

```
for v = 1:number of filaments
    load filament's coordinates

    calculate length of each bond on the chain
    calculate length of the current filament
    count how many bonds are on the filament
    calculate angles each bond makes with respect to the x-axis
    store calculated bond length, filament length, number of bonds and angles in matrices
    assign numbers of Fourier modes
    for i = 1:number of bonds
        calculate "mid-bond-length coordinates"
        for n = 1:number of Fourier modes
            calculate the amplitude of each Fourier mode
        end
    end
    for i = 1:number of bonds
        calculate Fourier angles for the current filament
    end
end

calculate average filament length, average number of bonds and average bond length
plot measured angles and angles from Fourier analysis vs mid-bond-length coordinates
calculate variance of each mode amplitude
assign guessed value for persistence length and pixelation error
find the best fit values for the persistence length and error value using nlinfit function
calculate theoretical variance
plot calculated variance and theoretical variance as a function of mode number
```

It is important to note that good initial guesses for the persistence length and error coefficient are important for the fits to converge to accurate estimates. For this, we use known values of filament persistence lengths from the literature and take ϵ_k to be of the order of the size of a single pixel.

2.2.5 Limitations of Fourier Analysis Technique

Fourier analysis has been a very useful tool in the past decade and it has been used in a number of studies, such as investigating velocity-dependent rigidity of microtubules [22], and study of bending dynamics of actin filaments and microtubules at thermal equilibrium [23]. However, the use of Fourier analysis for in *vivo* data presents challenges. For in *vivo* data, the number of microtubule or actin contours is limited, and obtaining accurate coordinate data from images presents a challenge. This technique also requires fluctuating microtubules to have similar length with both ends free to wiggle.

2.3 Curvature Analysis Technique

It has been recently shown that curvature distributions can provide useful information in characterizing microtubule deformation in cells [18, 19]. In this project, we explore this tool further and show how it can be equivalent to other existing methods.

2.3.1 Curvature Distribution for Semi-Flexible Chains

In the absence of intrinsic curvatures, the total energy of a filament, given by Eq. (2.3), can be written as,

$$U = \frac{1}{2} EI \int_0^L \left(\frac{d\theta}{ds} \right)^2 ds \ . \tag{2.35}$$

Both in simulations as well as in the interpretation of the experimental results, however, one typically uses a discretized model instead. To relate curvature distribution to the persistence length of bio-filaments, we then assume that our bio-filament is made of multiple rigid rods, equal in length. Using r_i as the position of the i^{th} point on the chain having coordinates be written as x_i and y_i, the unit tangent vector from the beginning to the end of each rod can be written as

$$t_i = \frac{1}{l} \left[(x_{i+1} - x_i)\, \hat{x} + (y_{i+1} - y_i)\, \hat{y} \right] \tag{2.36}$$

where

$$l = \sqrt{(x_{i+1} - x_i)^2 + (y_{i+1} - y_i)^2} \ . \tag{2.37}$$

Since t_i represents the direction along each rod, assuming that the angles between the rods are small, the equation for bending energy can be written in discrete form in terms of t_i and r_i, *i.e.*,

$$U = \frac{1}{2} EI \sum_{i=1}^{N-2} \frac{(t_{i+1} - ti)^2}{(r_{i+1} - r_i)^2} \Delta s \ . \tag{2.38}$$

The local curvature along the backbone of the chain can then be simply calculated as

$$\kappa_i = \frac{\theta}{(\Delta s_i + \Delta s_{i+1})/2} \ . \tag{2.39}$$

Assuming that the bending energy is the dominant energy, and using the fact that bond angles should be obey the Boltzmann distribution, one can show that curvatures are going to be distributed according to

$$P(\kappa_i) = \sqrt{\frac{L_p \Delta s}{2\pi}} e^{\frac{-L_p \kappa_i^2 \Delta s}{2}} \ . \tag{2.40}$$

Similar to curvatures, the distribution of bond angles obeys a Gaussian distribution,

$$P(\theta_i) = \sqrt{\frac{\Gamma}{\pi}} e^{-\Gamma\theta_i^2} \quad , \tag{2.41}$$

where $\Gamma = L_p/(2\Delta s)$

2.4 Effects of Coarse-graining on Curvature Distributions

Similar to Fourier analysis, noise plays an important role in the analysis of curvature from experimental images. It has been shown that errors introduced by pixelation can affect alter that measured curvature distributions, and therefore, filament contours have to be sub-sampled to minimize contribution to curvature distributions from noise [18]. This sub-sampling can be achieved either by skipping nodes, taking every m^{th} point, or regular decimation, taking every $(2^n)^{\mathrm{th}}$ point. This procedure is illustrated in Figure 2.4. In other word, one can write the relationship between m and n as

$$m = 2^n \quad . \tag{2.42}$$

The chain after decimation has fewer nodes, and the resulting distribution of angles after n decimations can be calculated as [24]

$$P(\theta^{(n)}) = \sqrt{\frac{\nu\Gamma}{\pi}} e^{-\nu\Gamma(\theta^{(n)})^2} \quad , \tag{2.43}$$

where ν is given by

$$\nu = \frac{1}{(2^{n+1}-1)(1-2^{-n})/3+1} \quad . \tag{2.44}$$

Writing the results in terms of curvatures one gets

$$P(\kappa^{(n)}) = \sqrt{\frac{\mu L_p \Delta s^{(n)}}{2\pi}} e^{-\mu L_p \Delta s^{(n)} (\kappa^{(n)})^2/2} \quad , \tag{2.45}$$

where the exponent μ is given by

$$\mu = \frac{2^n}{(2^{n+1}-1)(1-2^{-n})/3+1} \quad . \tag{2.46}$$

Note that in the limit of $n \to \infty$, $\mu = 3/2$ which implies $L_p \to (3/2)L_p$ in the limit of infinite number of decimations. This demonstrates that the effects on decimation can be drastic especially if one is interested in measuring the persistence length of the underlying chain.

2.4.1 Algorithm for Curvature Analysis Approach

In order to measure the curvature distributions, a Matlab algorithm was developed. The pseudo-algorithm for this code is given below.

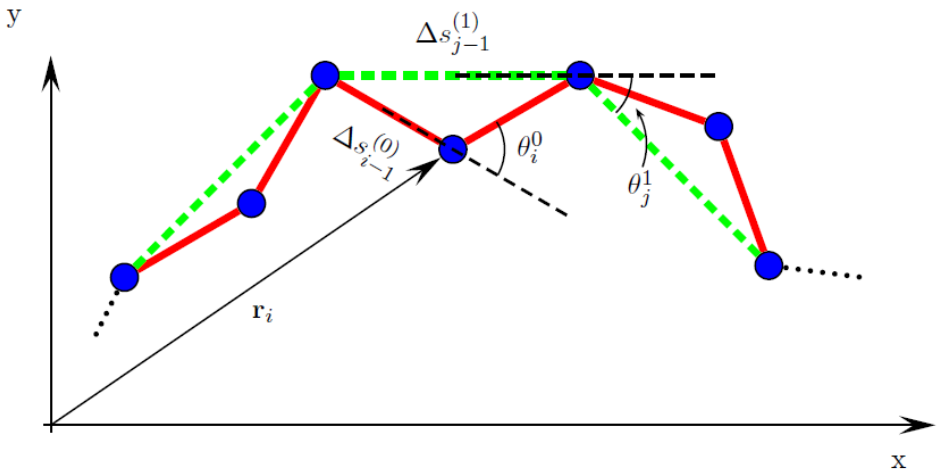

Figure 2.4: A discrete model of a microtubule. The variable θ_i^0 denotes the angle between consecutive bonds. $\Delta s_{i-1}^{(0)}$ is the spacing between neighboring coordinates $\vec{r}_{i-1}$ and $\vec{r}_i$. Dashed bonds (green) show the resulting chain as a result of decimating the coordinates once.

```
for v = 1:number of filaments
    load filament's coordinates
    calculate the spacing between adjacent x-coordinates
    calculate the spacing between adjacent y-coordinates
    calculate the length of each bond on the chain
    calculate the length of the current filament
    count how many bonds are on the filament
    calculate the angles each bond makes respect to the x-axis
    store calculated filament length in a matrix
    define how many nodes to skip over
    find last node for the skipping
    for i = 1:number of nodes
        calculate displacements in the x- and y-directions between the nodes
        calculate the bond length after skipping nodes
        store the bond length after skipping nodes
    end

    for i = 2:number of nodes-1
        calculate the position of each node of the sub-sampled filament
    end

    for i = 1:number of nodes
        calculate the length of the current bond
        calculate the length of the next bond
        calculate the angle each bond makes with the previous bond
        calculate curvature at each nodes
    end
end
plot histogram of curvatures
fit the histogram to a Gaussian distribution, and estimate the variance.
```

2.5 Summary

In this Chapter, we briefly explained the mechanics of bending. Then, the theory for Fourier analysis approach was also discussed in great detail. We showed how the variances of Fourier mode amplitudes are related to the persistence length. The errors caused by pixelation were discussed as well. The chapter ended with the discussion o the theory for curvature analysis approach. We also introduced the idea of decimation, which we will make use of in the following chapter.

Chapter 3

Results

After developing the algorithms for Fourier and curvature analysis approaches, the algorithms were used to analyze filaments generated using Monte Carlo simulations, in order to validate and compare. Then, both approaches were applied to the experimental data of actin gliding assays to measure the persistence length of the actin filaments. This chapter will discuss the results from those investigations.

3.1 Monte Carlo Simulations

In order to replicate a typical situation in an experiment, we generated chains by consecutively adding bonds with a bond angle distribution given by Eq. (2.41). For simplicity, we set the bond length to be 20 nm, which is equal for every bond. Figure 3.1 shows the shapes of some sample filaments generated from the simulations. The pseudo-algorithm for generating the chain generation is given below.

```
assign number of filaments, bond length and persistence length
for v = 1:number of filaments
    assign number of bonds
    set the first angle to zero
    calculate standard deviation for Gaussian distribution
    for i = 2:number of bonds
        if (i < number of bonds)
        calculate angle respect to the previous angle using the Gaussian distribution
        end
        calculate positions of the node using the calculated angle
    end
    write filament's coordinates to a file
end
```

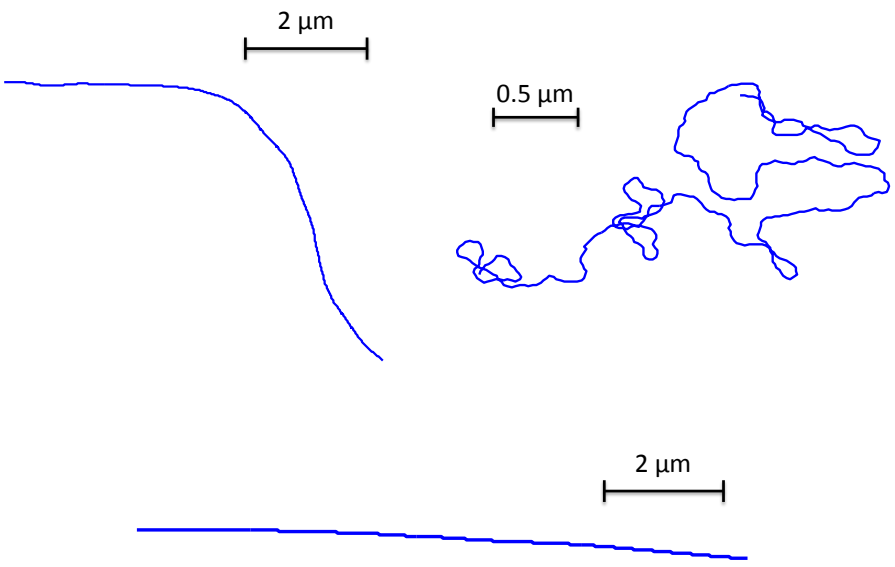

Figure 3.1: Sample filaments generated by the Monte Carlo simulation with different persistence lengths. Each filament has 500 nodes with the length of 10 μm. The top-left filament has a persistence length of 20 μm, which is the value for an actin filament. The top-right filament represents a very soft filament with a persistence length of 0.1μm. The bottom filament represent a microtubule-like filament with a persistence length of 1 mm.

3.1.1 Validation of Fourier Analysis Approach

In Chapter 2, the theory behind the Fourier analysis technique along with our algorithm for persistence measurement via this technique was discussed in detail. Nevertheless, before applying this technique to experimental data, the verification of our algorithm is required. Fourier analysis code was then applied to the filaments generated by the Monte Carlo simulation to confirm whether the obtained persistence length matches the given persistence length. Figure 3.2 shows that the angles produced by the measured mode amplitudes nicely match the original angles measured by the arctangent function along the filaments. This is evidence that our Fourier analysis technique perfectly replicated the generated filaments.

Then, the variances of the Fourier mode amplitudes are investigated against the mode numbers as shown in Figure 3.3. The log-log plot shows the linear relationship between the variance and mode numbers, which is consistent with the theory without taking account of the errors from pixelation. The theoretical variances calculated by substituting the known persistence length into Eq. (2.34) with no error term were also plotted on the same graph. Because the measured persistence length matches the input persistence length for filaments with persistence length greater than 0.3 μm, our Fourier analysis technique is successful in measuring the persistence length of the generated filaments. We also observed that variation in length of filaments has no effect on the variance plot (data not shown).

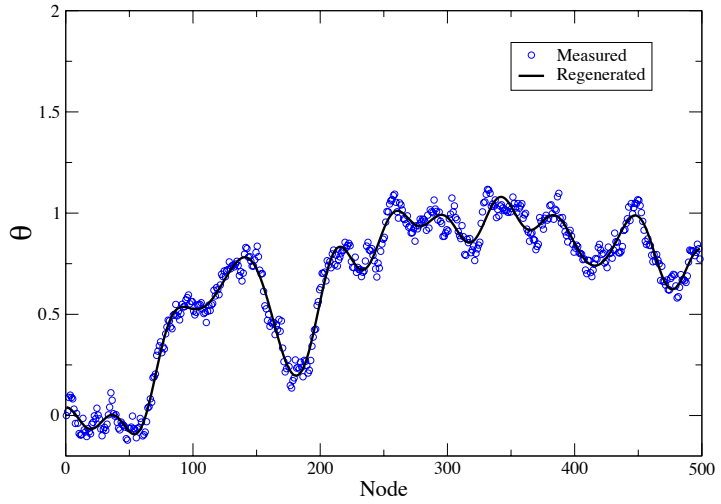

Figure 3.2: The regenerated angles from the measured mode amplitudes fits well with the measured angle for the filaments with persistence length of 17 μm, which is a rough approximation for the persistence length of actin filaments in literature [1].

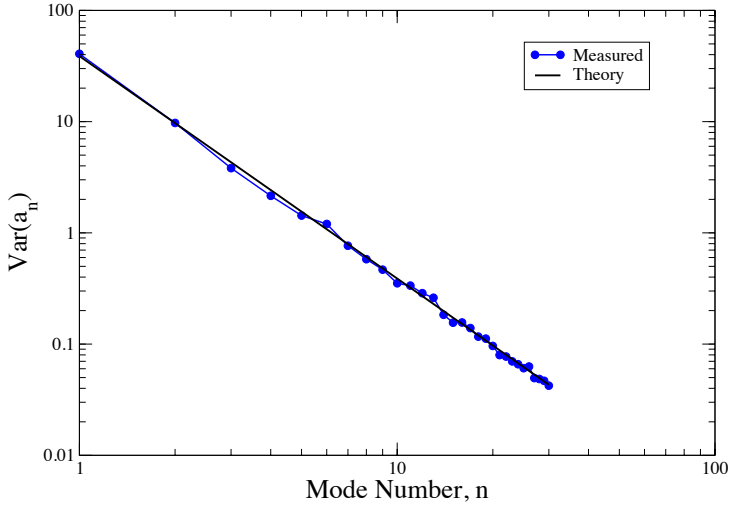

Figure 3.3: The log-log plot of the theoretical Fourier mode variances and measured variances against the Fourier mode numbers for a set of filaments with persistence length of 17 μm.

3.1.2 Validation of Curvature Analysis Approach

For a chain consisting of 500 nodes with persistence length of 17 μm, the resulting curvature distribution without decimation is shown in Figure 3.4 and as expected it is Gaussian with the correct persistence length, meaning that measured μ calculated from the Gaussian fit is consistent to the theoretical value calculated from Eq. (2.46). For no decimation, we measured μ to be 0.998, which is very close to the theoretical value of 1.000. If we now take

every other 32^{nd} node, *i.e.* decimate by 5, the measured curvature distribution is still a nice Gaussian as shown in Figure 3.5. The measured μ value is now 1.532, which is still consistent with the theoretical value of 1.499. This procedure can be continued for any decimation as long as the chains are long enough to measure the persistence length from decimation.

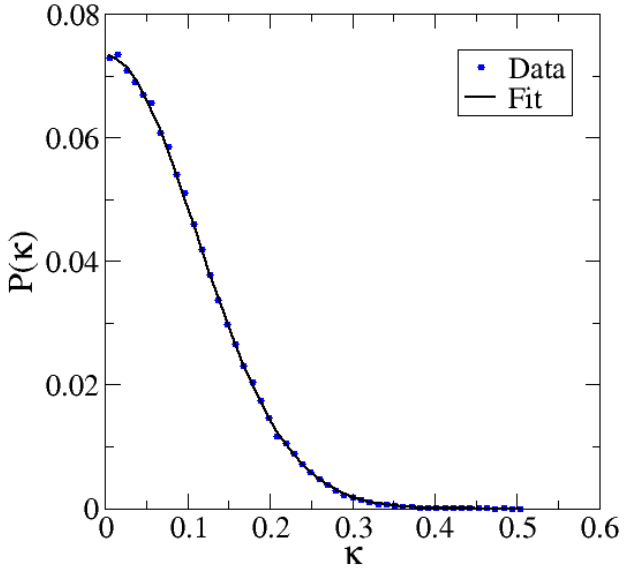

Figure 3.4: Curvature distribution measured without decimation for a 500-node chain with persistence length of 17 μm. Measured μ is obtained to be 0.998, which is very close to the theoretical value of 1.000.

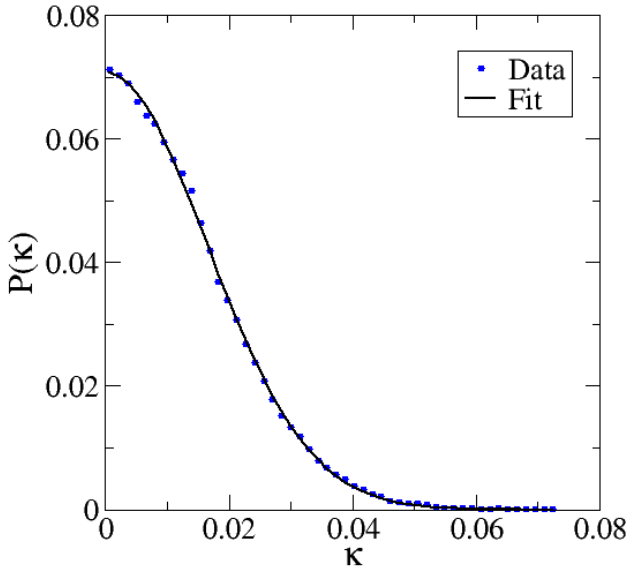

Figure 3.5: Curvature distribution measured after decimation by 5, or taking every 32^{nd} node, for a 500-node chain with a persistence length of 17 μm. Measured μ is obtained to be 1.532, which is very close to the theoretical value of 1.499.

To further investigate our curvature approach for persistence length measurements, the technique was applied to the generated filaments with various persistence lengths, from very stiff to very soft filaments. The other parameters, such as bond length and number of bonds, were set to be the same for every set of filaments. Our results show that the curvature approach performed very well for filaments with persistence length greater than 10 μm. Once the persistence length of the filaments was below 10 μm, measured μ started to deviate from theory. This behavior is shown in Figure 3.6. This deviation can be easily explained, since our theory assumes that the filament is very stiff. For this investigation, the curvature was also measured for every m^{th} nodes, where m can be related to the decimation n by $m = 2^n$, as discussed earlier in Chapter 2. Figure 3.6 also shows that measured μ is still consistence with theory, even though the curvature was taken for every m^{th} point instead of 2^n points.

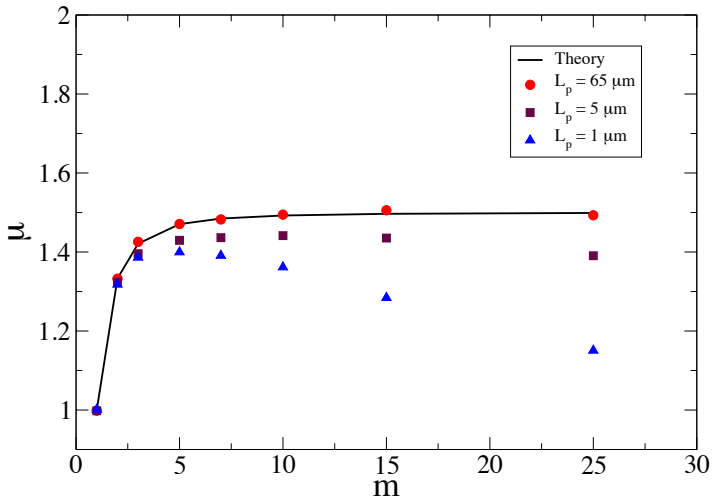

Figure 3.6: The measurement of μ for sets of filaments with various persistence lengths. Once the persistence length is less than 10 μm, measured μ deviates from theory (solid line).

3.1.3 Pixelation Effect

In experimental data, the monomer is typically smaller than the pixel size of the images. Thus, the information harvested from the image is not the actual position of the monomer but the position of the pixel that the monomer is in. Since the size of an actin monomer is approximately 3 nm, which is much smaller than our pixel size of 158 nm, the coordinates we obtained from our data do not represent the exact positions of the actin filaments, but it is the center of those pixels that our tracing code scans across (see section 3.2.1). To investigate this effect, filaments were created using the same approach as earlier, but with many more nodes. We then pixelated this data and used the coordinates of the pixels as our filament coordinates. The curvature analysis technique was again performed on this data to see the effect of pixelation on the "ideal" filaments. The plot in Figure 3.7 shows that measured μ starts very small and gets larger as the chain is sub-sampled. Nevertheless, the

increase in value tends to slow down after $m = 20$ and reach steady state. This shows that for the given pixel size, curvature measurements are dominated by noise for $m \leq 20$.

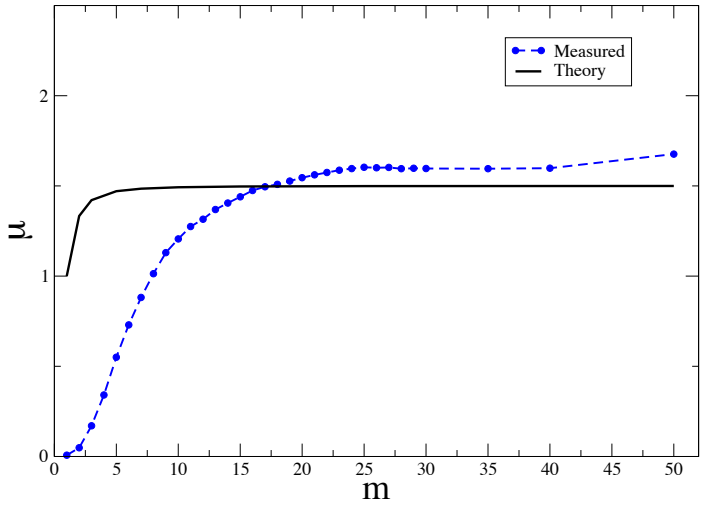

Figure 3.7: Measured μ value for the pixelated filaments with a persistence length of 13 μm. The curve corresponds to the result from experiment only in the low skipping number regime.

3.2 Estimation of Persistence Length from Experiments

3.2.1 Actin Gliding Assays

We conclude earlier that our curvature analysis technique performs nicely for filaments with a persistence length greater than 10 μm. Therefore, the most suitable bio-filaments for testing the curvature analysis technique are actin filaments, which are reported to have a persistence length of ~ 17 μm [1].

The ideal experimental setup would be looking at actin filaments fluctuating in a solution, using fast enough camera, and tracing the filaments in three dimensions. But that is very challenging since most microscopes have really slow acquisition times and the filaments tend to move in and out of focus. As a result, one typically gets blurry images. Thus, to avoid these problems, we instead turned to actin-gliding assays.

The experimental system we used was an *in vitro* actin gliding assays, performed by Prof. Vidali's group at WPI. In this system, actin filaments are attached to a glass surface by means of molecular motors. Since the motors used in the experiments were non-functional, the filaments stayed still like glued to the glass surface, allowing for easier imaging without the need for TIRF microscopy. Figure 3.8 shows a cartoon depiction of an actin gliding assays.

After obtaining the images of the filaments, we used in-house developed Matlab algorithm to identify the contours of the actin filaments. Since our Matlab algorithm can identify the contour for only one filament at a time, each filament was cropped using the ImageJ program

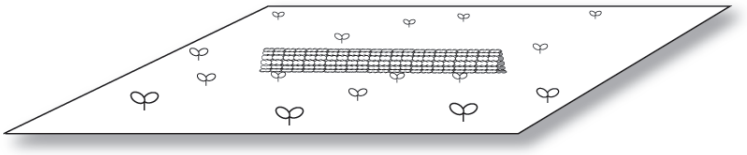

Figure 3.8: Cartoon shows the actin gliding assay experiment, where dead myosin motors are spread on the glass surface and act as a glue to attach the actin filaments to the surface.

and then saved as a new image. Then, the cropped filaments were traced for their contours using the Matlab algorithm by performing vertical scan along filament contour, and fitting the intensity profile to a Gaussian distribution. Then, the mean of that distribution was taken to be the filament position. Figure 3.9 illustrates a cropped filament with its traced contour displayed as a red line. The contour data for 435 filaments were obtained in total.

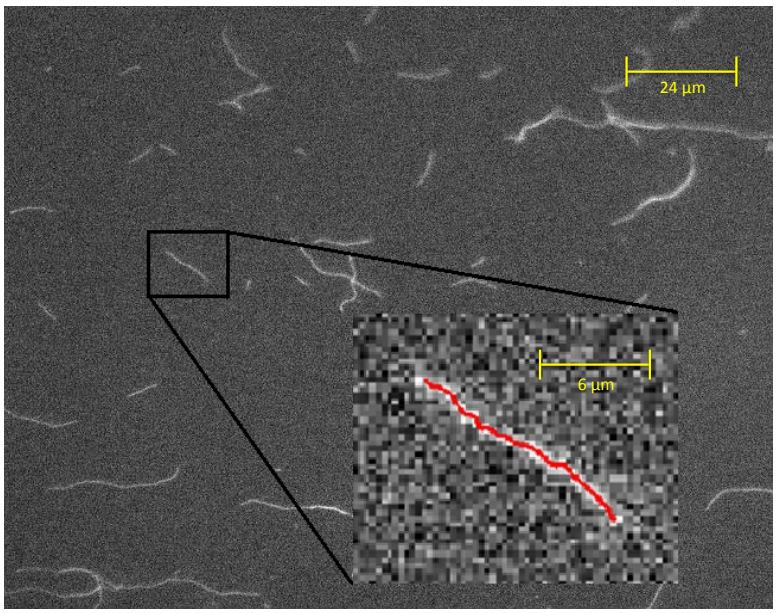

Figure 3.9: An experimental image form the actin gliding assay. Courtesy of Vidali Lab. The cropped image is shown in the smaller rectangular area with the filament traced contour displayed as a red line.

3.2.2 Measurement of Persistence Length using Fourier Analysis

After having a set of x-y coordinates of actin filaments from experiments, the Fourier analysis technique was performed on the data in order to find the persistence length. The algorithm for this technique is discussed earlier in Chapter 2. As shown in Figure 3.10, the measured variance plot displayed the error tail, caused by pixelation or the second term of Eq. (2.34). At first, we used *nlinfit* function in Matlab to obtain the best fit, but the values from the fit function poorly described the first few modes. Those first few modes were the most significant to analyze the curvature, since they hugely characterize the filament shape, moreover the latter modes were mostly governed by noise from the experiment. After several iterations, we determined the best fit persistence length to be 12.8 μm, which is consistent with the literature. Also, the *nlinfit* function gave the best fit for the pixelation error, ϵ_k, to be 0.47 μm. This persistence length value will be used as the basis value to determine the spacing for our curvature analysis approach.

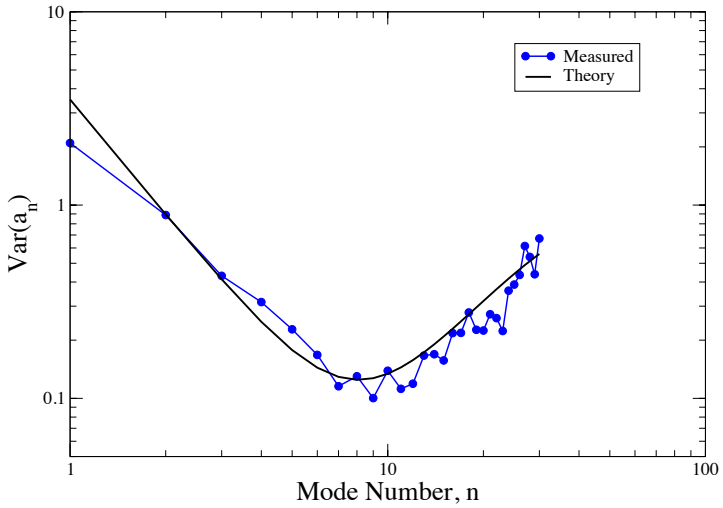

Figure 3.10: Log-log plot of the best-matched theoretical variance for the filaments with persistence length of 12.8 μm and the pixelation error constant of 0.47 μm and measured variance of an against the mode numbers for the set of experimentally actin filaments.

3.2.3 Application of Curvature Analysis

Equation (2.45) states that the curvature distribution with decimation depends on the bond spacing. It was discussed earlier in Chapter 2 that the pixel size of filament images obtained from experiments is much greater than the monomer. Performing decimation with known bond spacing greater than the pixel size is necessary for the curvature analysis approach in order to determine the persistence length of the filaments. For that, one needs to know the bond spacing first, and this can be obtained by performing our technique on a set of experimental data with known persistence length.

Since we obtained the persistence length using the Fourier analysis technique, it can be used to determine the spacing for our curvature analysis approach. After applying our curvature analysis approach to the experimental data, the curvature distributions for $n = 0$ deviated from the Gaussian distribution, as shown in Figure 3.11. This behavior is due to the presence of pixel noise. Nevertheless, for greater decimation, such as taking every 8^{th} point, a nice Gaussian distribution can be obtained, as shown in Figure 3.12. So, the curvature distribution can be successfully used for thermally-driven polymers.

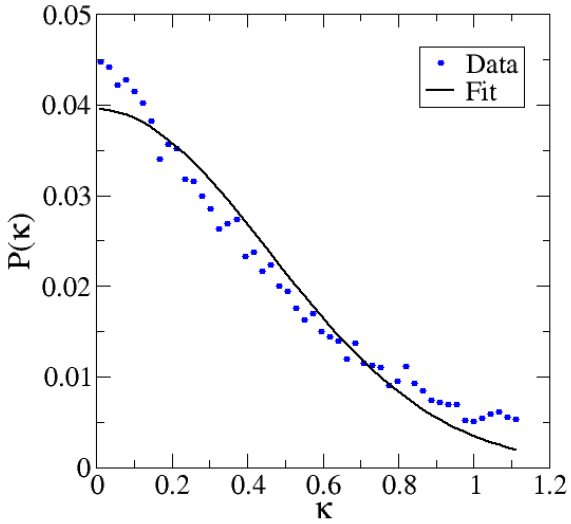

Figure 3.11: Curvature distribution for the experimental data with no decimation. Solid line shows a fit to a Gaussian distribution.

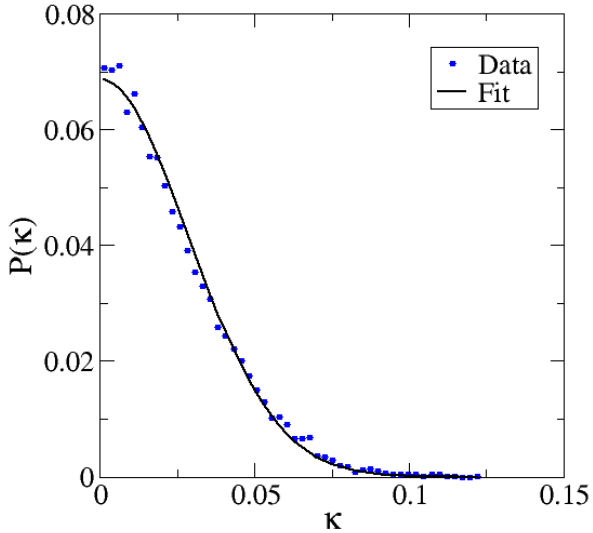

Figure 3.12: Curvature distribution for the experimental data, measured by taking every 8^{th} node on the filaments. Solid line shows a fit to a Gaussian distribution.

We then used the measured persistence length as our guessed value and observed the behavior of μ as a function of m. However, shown in Figure 3.13, the measured μ keeps on increasing without any sign of becoming steady. This behavior does not correspond to the result obtained from the generated filaments, where μ converges to 1.5.

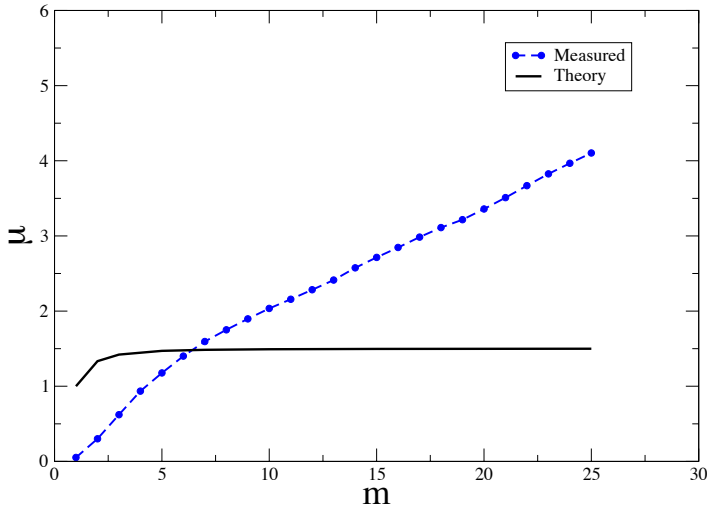

Figure 3.13: Measured μ against m for the experimental data using the estimated persistence length of 12.8 μm.

3.3 Summary

To validate and investigate the limitations of both Fourier and curvature analysis approaches, Monte Carlo simulations were used to generate the "ideal" filaments. Both techniques showed poor argument with theory on low persistence length filaments. The measured persistence length will start to deviate from the input persistence length when the input persistence length is below 0.3 μm for the Fourier analysis approach, and 10 μm for the curvature analysis approach. The pixelation effect was also investigated for the curvature analysis approach.

Both approaches were then applied to the experimental data of actin gliding assays. The persistence length of the filaments from the experiment was measured using the Fourier analysis approach, and found to be 12.8 μm, which is consistent with literature. However, the curvature analysis approach behaved unexpectedly with the experimental data. Even though the curvature distribution of those filaments was Gaussian, measured μ showed no sign of reaching steady state when decimation increases.

Chapter 4

Conclusions and Future Directions

In this project, we investigated in great detail a novel approach to analyze filament bending, namely curvature analysis, and compared it to a well-known method, Fourier analysis. In order to verify theoretical predictions on the scaling properties of curvature distributions, we performed Monte Carlo simulations in which polymer chains with known persistence lengths were created. We then used both the Fourier and curvature analysis approaches to measure the persistence length of these simulated filaments, and investigated the effects of experimental noise. As predicted from our calculations, the measured curvature distributions were Gaussian, and our theoretical calculations, which assumed stiff filaments, were valid for filaments larger than 10 μm. In comparison, both the Fourier and curvature methods were able to give accurate estimates of the persistence length. Thus, we can conclude that our curvature analysis approach can successfully analyze the ideal filaments, even in the presence of experimental noise.

We then used both approaches to measure persistence length from experimental data, in which the intrinsic spacing is not known. For experimental data, we used actin filament contours obtained from actin gliding assays performed by the Vidali Lab. In these assays myosin motors were only used to pin the filaments onto the glass surface, and ATP was depleted to suppress motor activity. We applied Fourier analysis technique to obtain the persistence length of these filaments. We then analyzed the same data again with our curvature analysis approach and used the obtained persistence length to find the intrinsic spacing. While we obtained Gaussian distribution of curvatures as predicted by theory, the measured scaling coefficient did not agree with theoretical predictions. We believe this is due to mode selection, *i.e.* actin filaments settling onto a given set of configurations on the glass surface, because of the presence of myosin motors. Since these would typically correspond to higher mode amplitudes, they would not affect the results of Fourier analysis, which gives importance to lower modes.

One of our future goals is developing a cross-grained model of actin gliding assays that incorporate bending dynamics and the myosin motors. With such a simulation, we will be able to investigate the role of myosin motor density on the measured persistence length, and make a fair comparison with theoretical predictions. We also aim to use TIRF microscopy to observe the fluctuating filaments directly, without the need for pinning via "dead" myosin motors. This experiment is closer to the ideal experimental setup than the actin gliding assays. These simulations and experiments will overall help further develop curvature dis-

tribution technique as a useful tool for characterizing deformations in living cells.

Bibliography

[1] Frederick Gittes, Brian Mickey, Jilda Nettleton, and Jonathon Howard. Flexural rigidity of microtubules and actin filaments measured from thermal fluctuations in shape. *J. Cell Biol.*, 120(4):923–934, 1993.

[2] Jonathon Howard. *Mechanics of motor proteins and the cytoskeleton*, volume 1. Sinauer Associates Sunderland, MA, 2001.

[3] Mariana Ruiz. "File:Animal Cell Structure"- *Wikimedia Commons*, April 2006.

[4] Thomas Kreis and Ronald Vale. *Guidebook to the extracellular matrix, anchor, and adhesion proteins*. Sambrook and Tooze Publication at Oxford University Press, 1999.

[5] Donald E Ingber. Tensegrity i. cell structure and hierarchical systems biology. *J. Cell Sci.*, 116(7):1157–1173, 2003.

[6] Bruce Alberts. *Essential cell biology: an introduction to the molecular biology of the cell*, volume 1. Garland Pub, 1998.

[7] Rob Phillips, Jane Kondev, Julie Theriot, Hernan Garcia, and Bernard Chasan. *Physical biology of the cell*, volume 78. Taylor and Francis Group, 2 edition, 2012.

[8] Zlira. "File:Microtubule_Id.svg" - *Wikimedia Commons*, December 2011.

[9] John Squire. The structural basis of muscular contraction. 1981.

[10] A Draeger, WB Amos, M Ikebe, and JV Small. The cytoskeletal and contractile apparatus of smooth muscle: contraction bands and segmentation of the contractile elements. *J. Cell Biol.*, 111(6):2463–2473, 1990.

[11] Boumphreyfr. "File:Actin Strand" - *Wikimedia Commons*, June 2009.

[12] Mikael Haggstrom. "File:Intermediate Filament" - *Wikimedia Commons*, January 2008.

[13] Julien Husson, Liedewij Laan, and Marileen Dogterom. Force generation by microtubule bundles. *Biophys. Rev. Lett.*, 4(01n02):33–43, 2009.

[14] Taviare Hawkins, Matthew Mirigian, M Selcuk Yasar, and Jennifer L Ross. Mechanics of microtubules. *J. Biomech.*, 43(1):23–30, 2010.

[15] Junko Mizushima-Sugano, Tadakazu Maeda, and Taiko Miki-Noumura. Flexural rigidity of singlet microtubules estimated from statistical analysis of their contour lengths and end-to-end distances. *Biochim. Biophys. Acta, Biophys. Incl. Photsynth.*, 755(2):257–262, 1983.

[16] Mahito Kikumoto, Masashi Kurachi, Valer Tosa, and Hideo Tashiro. Flexural rigidity of individual microtubules measured by a buckling force with optical traps. *Biophys. J.*, 90(5):1687–1696, 2006.

[17] Rick B Dye, Stephen P Fink, and RC Williams. Taxol-induced flexibility of microtubules and its reversal by map-2 and tau. *J. Biol. Chem.*, 268(10):6847–6850, 1993.

[18] Andrew D Bicek, Erkan Tüzel, Daniel M Kroll, and David J Odde. Analysis of microtubule curvature. *Methods in cell biology*, 83:237–268, 2007.

[19] Andrew D Bicek, Erkan Tüzel, Aleksey Demtchouk, Maruti Uppalapati, William O Hancock, Daniel M Kroll, and David J Odde. Anterograde microtubule transport drives microtubule bending in llc-pk1 epithelial cells. *Mol. Biol. Cell*, 20(12):2943–2953, 2009.

[20] David J Odde, Le Ma, Amelie H Briggs, Alyssa DeMarco, and Marc W Kirschner. Microtubule bending and breaking in living fibroblast cells. *J. Cell Sci.*, 112(19):3283–3288, 1999.

[21] Frederick Reif and F Reif. *Fundamentals of statistical and thermal physics*, volume 1. McGraw-Hill New York, 1965.

[22] Marcel E Janson and Marileen Dogterom. A bending mode analysis for growing microtubules: evidence for a velocity-dependent rigidity. *Biophys. J.*, 87(4):2723–2736, 2004.

[23] Clifford P Brangwynne, Gijsje H Koenderink, Ed Barry, Zvonimir Dogic, Frederick C MacKintosh, and David A Weitz. Bending dynamics of fluctuating biopolymers probed by automated high-resolution filament tracking. *Biophys. J.*, 93(1):346–359, 2007.

[24] Pattipong Wisanpitayakorn and Erkan Tüzel. in preparation.